iScience

CellPress
OPEN ACCESS

Article

Dendritic boron and nitrogen doped high-entropy alloy porous carbon fibers for high-efficiency hydrogen evolution reaction

Jin-Hua Liu, Jie Zheng, Mang Niu, ..., Ru Li, Jun Zhang, Yun-Ze Long

qdzhengj@qdu.edu.cn (J.Z.)
yunze.long@qdu.edu.cn (Y.-Z.L.)

Highlights

Quantum dot-sized HEA particles in nanofibers were synthesized

Dendritic nanofibers were prepared by carbonizing PAN for the first time

The dendritic nanofibers achieved low overpotential of 38.5 mV for HER

Liu et al., iScience 27, 109616
May 17, 2024
https://doi.org/10.1016/j.isci.2024.109616

iScience

CellPress
OPEN ACCESS

Article

Dendritic boron and nitrogen doped high-entropy alloy porous carbon fibers for high-efficiency hydrogen evolution reaction

Jin-Hua Liu,[1] Jie Zheng,[2,*] Mang Niu,[3] Xuehao Li,[1] Zhihan Gao,[1] Peng Wang,[1] Shuaijie Wang,[1] Rongxu Wang,[1] Seeram Ramakrishna,[4] Ru Li,[5] Jun Zhang,[1] and Yun-Ze Long[1,6,*]

SUMMARY

Among various electrocatalysts, high-entropy alloys (HEAs) have gained significant attention for their unique properties and excellent catalytic activity in the hydrogen evolution reaction (HER). However, the precise synthesis of HEA catalysts in small sizes remains challenging, which limits further improvement in their catalytic performance. In this study, boron- and nitrogen-doped HEA porous carbon nanofibers (HE-BN/PCNF) with an *in situ*–grown dendritic structure were successfully prepared, inspired by the germination and growth of tree branches. Furthermore, the dendritic fibers constrained the growth of HEA particles, leading to the synthesis of quantum dot-sized (1.67 nm) HEA particles, which also provide a pathway for designing HEA quantum dots in the future. This work provides design ideas and guiding suggestions for the preparation of borated HEA fibers with different elemental combinations and for the application of dendritic nanofibers in various fields.

INTRODUCTION

The depletion of traditional energy sources and environmental issues have posed significant challenges to human development, necessitating the development of green and renewable energy sources.[1–3] Hydrogen is primarily prepared through a water splitting process, widely considered the ultimate clean energy due to its sustainability, high energy density, and lack of byproducts,[4–6] but requires energy input to overcome potential obstacles in the electrochemical process and produce hydrogen and oxygen from water.[7] Platinum group noble metal-based catalysts are considered the most efficient HER catalysts due to their optimal hydrogen binding energy and other advantages.[8,9] Constrained by high prices and reserves, cost and availability need to be considered. Transition metal-based catalysts have garnered considerable attention owing to their abundant resources and cost-effective synthesis.[10] However, the catalytic performance of these catalysts still lags behind that of commercial counterparts.[11–13]

Based on classical catalytic theory, nanostructures can be constructed by introducing vacancies or defects, as well as alloying and crystal phase engineering to regulate surface metal sites, thereby regulating the hybridization process between 2p and 3d orbitals. The introduction of effective metal species, such as high-valent metals and noble metals, can not only regulate the local coordination environment and electronic structure but also create the heterogeneous phase, which can effectively enhance catalytic performance. Another way to increase catalytic activity is to introduce manufacturing defects such as non-metal N, B, P, etc. The defects can increase the number of charge off-domains or edge sites. Element B, characterized by its low atomic radius, possesses greater ease in infiltrating the interstitial spaces within the metal lattice, thereby inducing alterations in the crystalline structure of the composite material compared to P/S. However, an understanding of the structure-activity relationship is still lacking due to the small size, random distribution, and low boron content in the metal lattice.[14] High-entropy alloys (HEAs) as a solid solution structure, possess excellent hardness, toughness, corrosion resistance, and thermal stability due to their high configuration entropy, lattice distortion, sluggish diffusion, and cocktail effects.[15–17] Defects, edge sites, vacancies, and crystallinity always work together to form efficient interfaces, enhance synergistic effects optimize the adsorption of intermediates, and change the electronic structure.[18–20]

[1]Collaborative Innovation Center for Nanomaterials & Devices, Innovation Institute for Advanced Nanofibers, College of Physics, Qingdao University, Qingdao 266071, P.R. China
[2]Industrial Research Institute of Nonwovens & Technical Textiles, Shandong Center for Engineered Nonwovens (SCEN), College of Textiles Clothing, Qingdao University, Qingdao 266071, P.R. China
[3]State Key Laboratory of Bio-fibers and Eco-textiles, Institute of Biochemical Engineering, College of Materials Science and Engineering, Qingdao University, Qingdao 266071, China
[4]Center for Nanotechnology & Sustainability, Department of Mechanical Engineering, College of Design and Engineering, National University of Singapore, 9 Engineering Drive 1, Singapore 117576, Singapore
[5]Instrumental Analysis Center, Qingdao University, Qingdao 266071, P.R. China
[6]Lead contact
*Correspondence: qdzhengj@qdu.edu.cn (J.Z.), yunze.long@qdu.edu.cn (Y.-Z.L.)
https://doi.org/10.1016/j.isci.2024.109616

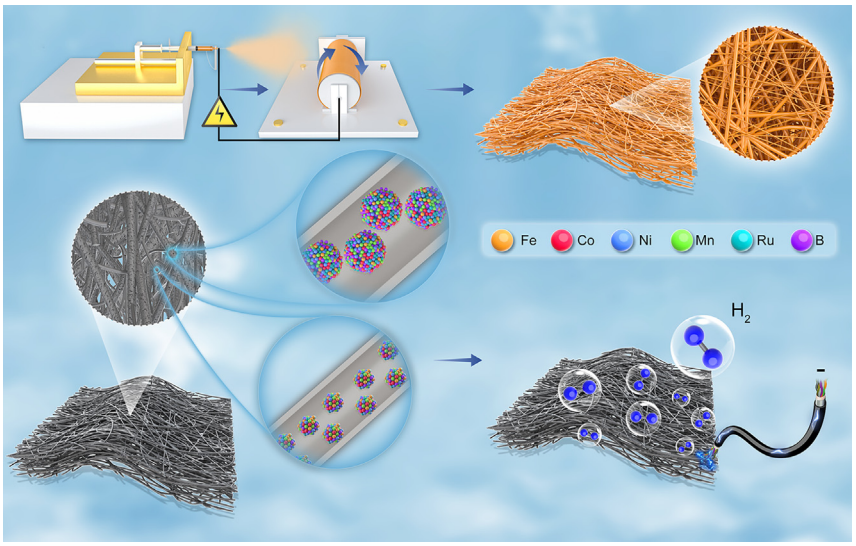

Scheme 1. Illustration of the synthesis of HE-BN/PCNF

In addition, most catalysts currently require the addition of binders to prepare solutions and drip them onto the carrier, resulting in uneven distribution. Carbon nanofibers (CNF) prepared by electrospinning have large specific surface areas, simple manufacturing processes, high aspect ratios, and good mechanical.[21] Nanofibers often possess a self-supporting structure after carbonization, making them suitable for loading catalysts and improving electrochemical performance.[22] Special structures such as multi-channel, porous, and hollow structures can increase the specific surface area by generating defects on the fiber surface,[23] but cannot break through the limitations of a single fiber. The nanonets and dendritic nanofibers are widely explored in the field of filtration due to their large contact area, extremely fine fiber diameter, and small pore size, which can significantly improve the screening of particles. At present, the formation of nanonets and dendritic fibers is attributed to the phase separation of charged droplets. Only when both jet and droplet are generated at the tip of the Taylor cone, nanonets and dendritic fibers can be generated, which is closely related to droplet charge density, humidity, and collector. However, the materials used to prepare nanonet/tree-like nanofiber are mainly several special polymers such as polyamide, poly(*m*-phenylene isophthalamide), polyurethane, and polyvinylidene fluoride (PVDF).[24,25] These polymer nanofibers cannot be carbonized at high temperatures and used in the field of electrochemical energy. Most of the carbon fibers used for electrochemical energy are obtained by carbonization of polyacrylonitrile (PAN), and it is a challenge for the industry to make PAN-based CNF break through the limitations of a single fiber and maintain their shape after carbonization.

In this work, B- and N-doped HEA porous dendritic carbon nanofibers (HE-BN/PCNF) via PAN-based carbonization were successfully prepared for the first time. In addition, the formation of HEAs was limited due to the formation of dendritic structure, and quantum-dot-sized HEAs in nanofibers (with an average diameter of 1.67 nm) were synthesized, which also provided ways to design HEA quantum-dot nanofibers in the future. The effect of element B on the HER catalysis of HEA carbon fibers was investigated in detail. The introduction of element B could enter the fibers and penetrate into the lattice of HEA, and it is also key to the generation of dendritic fibers. The introduction of boron allows the fibers to differentiate and germinate to form a dendritic structure, and the generation of dendrites allows the fibers to differentiate into more contact sites. The PCNF accelerates the transport of electrons and ions, thereby lowering the kinetic reaction barrier, and moderates the electronic configurations and optimizes thermodynamic hydrogen adsorption/desorption on the surface of the catalyst, which is responsible for the improved electrocatalytic efficiency. We believe that dendritic fibers are one of the future research directions for HEA nanofiber catalysis, and the present work will also provide design ideas for the preparation of boronized HEA fibers with other element combinations.

RESULTS

Materials synthesis and characterizations

The synthetic strategy of situ BN element-doped HEA porous dendritic carbon nanofibers is demonstrated in Scheme 1. PAN, PMMA, metal salt, and boric acid of different proportions were dissolved in DMF to prepare a mixed solution and then electrospinning was used to obtain a precursor nanofiber membrane (Figure S1). Figures S1A and S1B show pure metal salts precursor nanofibers with a small diameter (239 nm, Figure S3A). When a small amount of boric acid was added, the nanofibers became coarser in diameter (Figures S1C and S3B), and with further introduction of boric acid (Figures S1D–S1F), the nanofibers became even larger in diameter (Figures S3C–S3F), with filamentous fine fibers differentiated on the surface. The numbers and lengths of filamentous fibers increased with the increase in boric acid. This suggests that boric acid was successfully introduced into the nanofibers and altered the growth process, causing the fibers to differentiate into filaments. This may be due to the increase in the charge density of the polymer solution droplets induced by the electrospinning process, leading

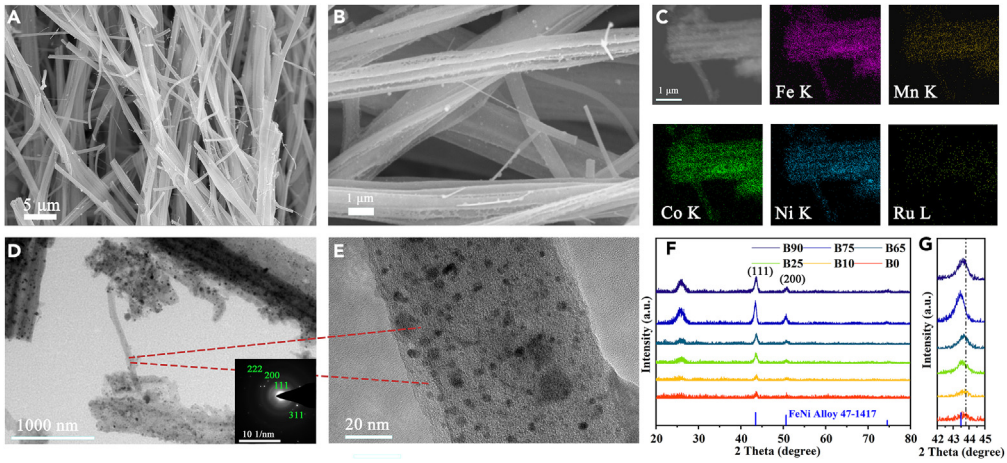

Figure 1. Physical characterizations of HE-BN/PCNF

(A and B) SEM images of HE-B_{75}N/PCNF.

(C–E) TEM and mapping images of HE-B_{75}N/PCNF.

(F) XRD patterns of HE-B_0N/PCNF, HE-B_{10}N/PCNF, HE-B_{25}N/PCNF, HE-B_{65}N/PCNF, HE-B_{75}N/PCNF, and HE-B_{90}N/PCNF.

(G) Enlarged XRD patterns.

to an increase in the instability of the charged droplets, resulting in more cleavage occurring after convergence in the Taylor cone.[26] Interestingly, this mechanism is different from the way nanofibers grow nanowires, as shown in Figures S1E and S1F, where the growth of filamentary fibers on the surface of the main fibers does not stop. The filamentary fibers differentiate again lengthen, and continue to lengthen, resulting in the filaments undergoing cross-linking. When boric acid is in excess (Figures S1G–S1I), the main fibers thicken to form beads, and the crosslinked filamentous fibers converge and become knotted to form a net. This morphology is different from the reported nanonet fibers so far,[26] and the netting is formed by the differentiation and growth of the main fibers, resulting in randomness.

The precursor nanofiber film is then carbonized to form a single-phase HEA solid solution dendritic porous nanofiber (Figures S2A–S2F). Compared to the precursor fiber membrane, the diameter of the carbonized fibers becomes smaller (Figure S3G), and the fiber surface exhibits a porous and multi-channel structure, which is conducive to the generation of more reactive active sites. With the introduction of boric acid, tiny fiber shoots begin to differentiate on the surface of the porous nanofibers (Figure S2C), and when the amount of boric acid is further increased, the shoots gradually grow and lengthen to become dendritic (Figures 1A, 1B, S2D, and S2E). Interestingly, the same doping concentration exhibits two morphologies, where Figures 1A and 1B shows thicker main fibers with a large number of branches on the surface, while Figure S2E shows finer main fibers with a large number of shoots on the surface. This also verifies the process of shoot growth under the doping concentration, and the two different morphologies resemble a mature tree and a thriving tree. The growth mechanism of carbonized fibers and precursor fibers is different. Despite filament splitting on the surface of precursor fibers, the surface of single fibers is smooth without fluffy shoots. This is because some of the synthesized HEA particles precipitated on the surface of the fibers during the carbonization process and interacted with boron, carbon, and nitrogen to form shoots. As the boron content increases and the fibers further form, it allows the shoots to gradually grow, forming branches of varying lengths on a single fiber. Similarly, excess boric acid causes the carbonized fibers to appear as beaded structures and dendritic knotted networks (Figure S2F). TEM and scanning transmission electron microscopy-energy dispersive X-ray spectroscopy (STEM-EDX) elemental mapping images (Figures 1C and S2G–S2K) verify the multi-channel dendritic fibers as well as the homogeneous distribution of elements including Fe, Co, Ni, Mn, Ru, B, C, N, and O.

High-resolution TEM (HRTEM) images show that a large number of HEA particles are densely and uniformly anchored in the PCNF (Figures 1D, 1E, and S4A–S4I). As the fiber thickens, the size of the HEA particles anchored to the fiber increases (Figures S3H and S3I). Figures S4B and S4C show that HE-B0N/PCNF consists of graphitized carbon and amorphous carbon at the lattice edge with a spacing of 0.37 nm, consistent with the (002) graphitic carbon crystal face.[27] The HEA particles have a clearly visible lattice fringe of 0.26 nm corresponding to the (111) plane. HE-B_{25}N/PCNF has a crystal face spacing of 0.21 nm corresponding to the (111) plane (Figures S4D and S4E). Figures 1D and 1E also confirms the presence of dendritic fibers, and the selected area electron diffraction (SAED) pattern (Figure 1D inset) demonstrates that the HEA particles exhibit characteristic crystal faces (111) and (200). Figure 1E is an enlarged image of Figure 1D, and it can be that the particle size of the HEAs on the branches become smaller, with an average size of 1.67 nm (Figure S5). The thickened main fiber expands the boundary conditions and makes the HE particles larger, while the slender dendritic structure shortens the boundary conditions and confines the growth of HE particles to a limited area. Therefore, the size of the HEA particles is optimized, which also provides ideas and methods for the future design of HE quantum dots based on nanofibers. Figure S4I shows the SAED of the branch nanofibers, where diffraction rings in the SAED pattern and lattice stripes in the HRTEM image gradually become blurred, indicating the transition from complete crystallization to amorphous.[28] Figure S6 shows the interplanar spacing statistics of HEA quantum dots in HE-B_{75}N/PCNF, which show the characteristic crystal planes of 0.209 nm (111) and 0.16 nm (200). High-angle annular dark-field scanning transmission electron microscopy (HAADF-STEM) also

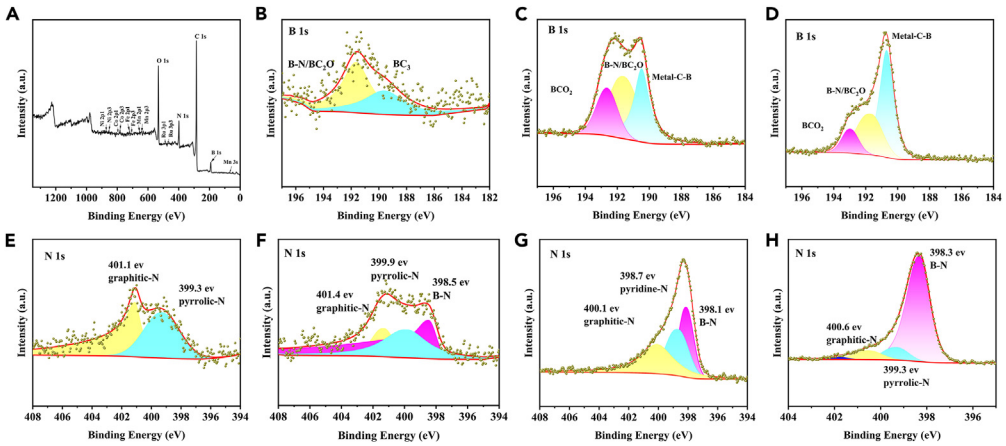

Figure 2. X-ray photoelectron spectroscopy characterizations of HE-BN/PCNF

(A) Survey spectrum of HE-B_{75}N/PCNF.

(B–D) B 1s of HE-B_{10}N/PCNF, HE-B_{75}N/PCNF, HE-B_{90}N/PCNF.

(E–H) N 1s of HE-B_0N/PCNF, HE-B_{10}N/PCNF, HE-B_{75}N/PCNF, HE-B_{90}N/PCNF.

shows a uniform distribution of HEA particles in the branch fibers (Figure S7). The proportion of amorphous carbon and graphitized carbon on the HE-B_{90}N/PCNF surface (Figure S4F) further increases due to the formation of beaded main fibers and networked fine fibers.

The XRD patterns (Figures 1F and 1G) show three distinct peaks at 26°, 43°, and 50°, respectively. They correspond to graphite (002 planes)[27] and iron-nickel alloys (111 and 200 planes) of the fcc phases (PDF#47–1417), respectively.[23] No XRD peaks from Fe, Co, Ni, Mn, Ru, or metal oxide separation were observed, indicating the formation of a single-phase HEA.[29] Boron can be decomposed into metal oxides by carbothermic reduction to form borides, as shown in Equations 1 and 2:[30]

$$MeO + B + C \rightarrow MeB + B_xO_y + CO \quad \text{(Equation 1)}$$

$$MeO + B_{13}C_2 \rightarrow MeB + CO \quad \text{(Equation 2)}$$

Compared with HE-B_0N/PCNF, the lattice of HE-B_{10}N/PCNF with low boron doping is almost unchanged. With the increase of boron content, more boron elements participate in the reaction to reduce metal oxides, resulting in more HEA particles and HEA metal borides, so that the peak position of the (111) and (200) planes moves slightly to a lower angle. XRD only shows the peak value of FeNi, so the borated layer should be amorphous or poorly crystalline.[31] In addition, the widening of the peak (111) indicates that B incorporation can lead to amplification of the FeNi lattice.[32] Because boron is more electronegative than Ni, Co, and Fe, electrons are transferred from the metal center to the B atom, facilitating the formation of the amorphous transition metal borides structure.[19] These amorphous B-containing substances prevent the growth and oxidation of nano-sized crystalline nuclei in HEA particles, which is also the reason for the synthesis of HEA quantum dots. In addition, the obvious increase of the carbon peak of 26° graphite also indicates the successful introduction of B element and its combination with C, and N to form graphitized carbon and amorphous carbon.

XPS is another technique that provides information to further understanding of the surface element composition of the sample as well as the valence state of the element. All the binding energies (BEs) were calibrated by the C 1s peak at 284.6 eV Figure 2A shows the XPS survey spectrum of HE-B_{75}N/PCNF. It can be seen that the material contains elements Fe, Co, Ni, Mn, Ru, B, N, C, and O, indicating the successful preparation of the material. Figures 2B–3D shows the spectra of XPS measurements based on different boron content. B1s can be deconvolved at 189.6 eV, 190.5 eV, 191.7 eV, and 192.7 eV, corresponding to BC_3, Metal-C-B, B-N/BC_2O, and BCO_2, respectively.[33,34]

The XPS of HE-B_{10}N/PCNF did not find Metal-C-B, which indicates that when a small amount of boron is introduced into the fiber, the boron element first combines with the C, and N element and does not enter the HEA lattice. The XRD images of HE-B_{10}N/PCNF and HE-B_0N/PCNF are almost identical, which also verifies this result. When the amount of boron is increased, the boron element and the high entropy metal form a metal-C-B bond. With the increase of boron element, the ratio of metal-C-B and B-N/BC_2O bond also increases, and the BC_3 level disappears suggesting electron donation from metal and B atoms to C atoms. The Metal-C-B and B-N/BC_2O ratios of HE-B_{75}/PCNF are approximately equal, so the electrochemical synergies effect is the best. However, excessive boron elements in HE-B_{90}N/PCNF will form more Metal-C-B bonds, which is not conducive to the synergistic effect of HEA and B-N. Figures 2E–3H shows the four fitted peaks in the N1s spectra with different boron contents, corresponding to graphite N bonds (401.6 eV), pyrrole N bonds (399.8 eV), pyridine N bonds (398.5 eV), and B-N bonds (398.1 eV), respectively.[34,35] N doping with porous nanofibers can improve the conductivity of the catalyst, accelerate the transport of electrons and substances, and avoid the aggregation of nanoparticles. B-N bonds, graphite N bonds, pyrrole N bonds, and pyridine N bonds can affect the charge delocalization of carbon, thereby improving the conductivity of the material.[35] The presence of pyridine N atoms at the carbon edge can also reduce the adsorption barrier of reactants on adjacent carbon atoms.[36] The O 1 s spectrum

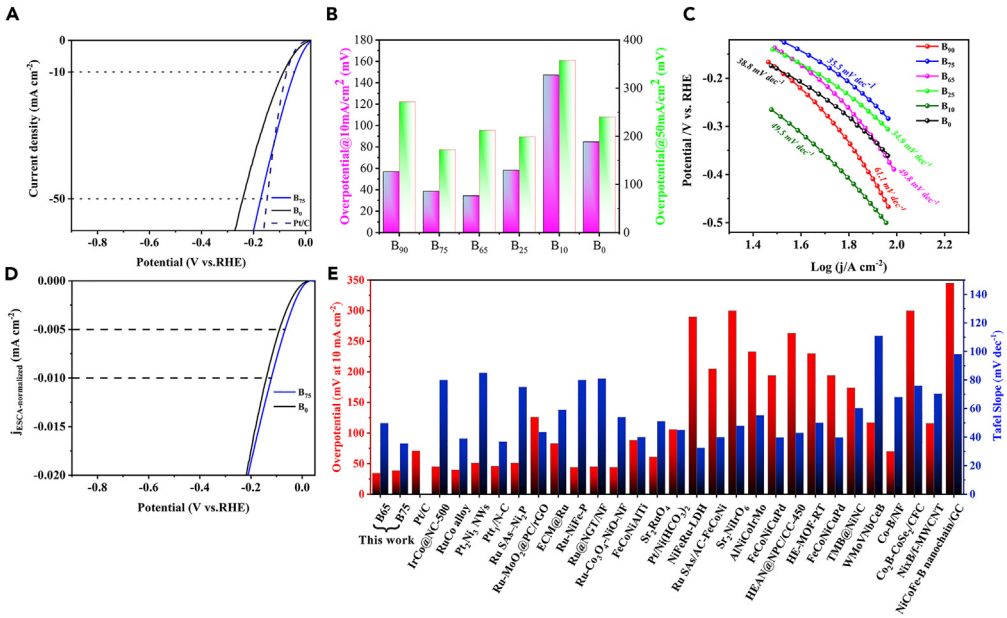

Figure 3. Electrocatalytic HER performance

(A) LSV curves.

(B) The corresponding histogram of overpotentials at 10 mA cm^{-2} and 50 mA cm^{-2}.

(C) Tafel slopes and (D) ECSA-normalized LSV curves of HE-B_0N/PCNF, HE-B_{10}N/PCNF, HE-B_{25}N/PCNF, HE-B_{65}N/PCNF, HE-B_{75}N/PCNF, and HE-B_{90}N/PCNF in 1.0 M KOH electrolyte.

(E) Comparison of HER overpotentials and Tafel slopes at 10 mA cm^{-2} in 1.0 M KOH for different catalysts. Those recently reported literatures for HER electrocatalysts were shown in Table S2.

(Figures S8A–S8D) reveals peaks at 531.8 and 532.8 eV, which are ascribed to hydroxyl groups and residual oxygen-containing groups on the surface, respectively.[37] Figures S8E–S8H suggests the coexistence of Mn^{2+} $2p_{3/2}$ (641.6 eV), and Mn^{3+} $2p_{1/2}$ (654.1 eV).[29] The Ru 3p XPS spectrum (Figures S8I–S8L) exhibits only metallic Ru states (461.4 and 484.8 eV for Ru^0 $3p_{3/2}$ and Ru^0 $3p_{1/2}$).[38] Compared to HE-B_0N/PCNF, the OH - shifted to a higher value after boronization, and the proportion of Ru and Mn metals at high energy levels increased. This positive shift can be attributed to the electronegativity of B inducing the formation of a higher oxidation state in the metal center or lowering the electron density around it.[19] The introduction of boron into the composition of the fibers expands the diameter of the fibers, which further reduces the mass ratio of the metal elements per unit area, and in addition, boron interacts with elements such as Fe, Co, Ni, to form the magnetic properties of the samples, which makes the peak fitting of the FeCoNi elements less obvious. These results reveal strong electronic interactions and charge distributions between the constituent elements, which enhance the catalytic activity of the metal sites.[28,39]

HER performance

In order to investigate the effect of the boron element on the electrochemical properties of high entropy alloy nanofibers, all the prepared catalysts were tested as working electrodes in a three-electrode system. Hg/HgO and graphite rod were used as reference electrode (RE) and counter electrode (CE). HER was tested inside a 1M KOH electrolyte and all potentials were calibrated with a reversible hydrogen electrode (RHE).

As shown in Figures 3A, 3B, and S9A, HE-B_{75}N/PCNF can achieve overpotentials of 38.5 mV and 172.1 mV at 10 mA cm^{-2} and 50 mA cm^{-2}, respectively. The performance outperforms other boron-doped ratios and pure high entropy alloys PCNF. The HE-B_{65}N/PCNF possesses superior performance to HE-B_{75}N/PCNF at 10 mA cm^{-2}, but it performs poorly at higher current densities. Interestingly, HE-B_{10}N/PCNF exhibits worse HER performance than HE-B_0N/PCNF, whereas HE-B_{90}N/PCNF shows better HER performance than HE-B_0N/PCNF. This discrepancy is because HE-B_{10}N/PCNF thickens the fiber diameter without generating dendritic fibers. In contrast, HE-B_{90}N/PCNF produces thicker fibers but still outperforms HE-B_0N/PCNF at 10 mA cm^{-2} due to the presence of entangled dendritic fibers. Figure 3C indicates that HE-B_{75}N/PCNF has the lowest Tafel slope (35.45 mV dec^{-1}), signifying faster electron transfer, which is superior to the other listed alloys. The Tafel slope reveals the mechanism of HER; a value close to 39 mV dec^{-1} indicates that the discharge reaction is rapid and the electrochemical desorption (Heyrovsky reaction) is the rate-limiting step.[7] The electrochemical impedance spectrum, displayed in Figure S9B, shows the electrode presenting a characteristic semicircle.

To evaluate the active site and intrinsic activity of the prepared electrocatalyst, the electrochemical surface area was measured (Figures S10 and S11A) using the double-layer capacitance (C_{dl}) method.[23] The increase in C_{dl} values indicates the generation of more electrocatalysis active regions.[40] The introduction of boron offers numerous reaction sites, such as boundaries, points, line defects, discordant sites, and

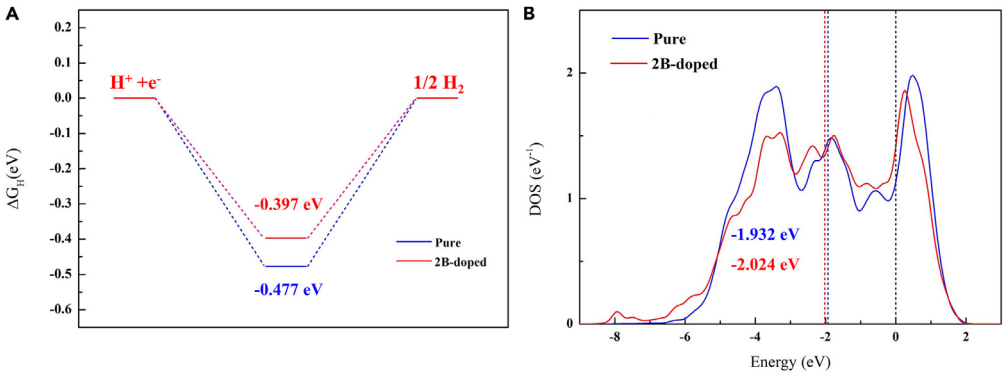

Figure 4. Density functional theory calculations

(A) The optimal free energies of H adsorption in pure alloy and 2B-doped alloy.

(B) The DOSs of Ru-4d in pure alloy and 2B-doped alloy. Energy zero was set as Fermi level and displayed with a black dashed line. The d-band centers of Ru-4d in pure alloy and 2B-doped alloy were displayed with blue and red dashed lines, respectively.

edges on the catalyst. Notably, HE-B_{75}N/PCNF does not have the maximum C_{dl} value, reinforcing that its optimal performance results from the synergistic catalytic effect of multiple action modes. The ECSA-normalized LSV curves (Figures 3C and S11B) and accompanying data (Table S1) demonstrate the high intrinsic HER activity of the compounds. Moreover, the overpotentials required for a current density of 10 mA cm^{-2}, when compared with recently reported HER electrocatalysts in 1M KOH electrolytes (Table S1) highlight the exceptional activity of HE-B_{75}N/PCNF. The chronoamperometric curve (Figure S12) demonstrated that high entropy materials have good stability. We then performed characterizations of the catalyst after stability test. The Raman spectra and XRD reveal that HE-B_{75}N/PCNF exhibit no obvious change after the durability test(Figure S13). Interestingly, the SEM image shows the diameter of dendritic fibers enlarged after long-term stability. The exact microstructure change still need further study.

DISCUSSION

Mechanism investigations

We performed density functional theory (DFT) calculations to reveal the mechanism of HER enhancement in B-doped alloys. As displayed in Figure S14A, there are nine kind of surface Ru atoms in pure alloy. The calculated free energies of H adsorption (ΔGH) on these surface Ru atoms are summarized in Figure S15, and the corresponding adsorption geometries are displayed in Figure S16. It is found that the optimal ΔGH in pure alloy is −0.477 eV, with H atom adsorbed at the hollow site of Ru-01 atom and two adjacent Ni atoms. Through structural optimization of different configurations (named Ru-01∼ Ru-09) and free energy (ΔGH) calculation as shown in Figure S15 and in Figure S16, we obtained the lowest energy stable HEA configuration (Ru-01) from the nine initial configurations. Based on this most stable HEA configuration, we started the calculation of B-doping. For B-doped alloys, B atoms were inserted at the hollow sites below the Ru-01 atom. Figures S14B–S14D shown the optimized structures of 1B-doped, 2B-doped and 3B-doped alloys. The calculated ΔGH on surface Ru-01 atoms in B-doped alloys are summarized in Figure S17, and the corresponding adsorption geometries are displayed in Figure S18. The ΔGH of 1B-doped, 2B-doped and 3B doped alloys are −0.426 eV, −0.397 eV and −0.561 eV, respectively. Therefore, 2B-doped alloy is the most ideal HER catalyst. This corresponds to the increasing doping of B from B_0 to B_{90} during the experiment. The decreased activity in HER performance in 3B-doped alloy could be attributed to the large structural deformations after doping, which enhanced the adsorption of H atom. The theoretical results here further indicate that the greater the amount of B doping is not the better, which is consistent with the results described in the experimental part. Moderate doping of B can produce more fiber branches and finer fibers, increase the exposed area and active site of the catalyst, and improve the catalytic performance. However, excessive doping of B increases the possibility of catalyst aggregation and makes the fiber branches thicker. It is not conducive to the improvement of catalytic performance, which can also be demonstrated in Figures S1 and S2. As displayed in Figure 4A, 2-B doping below Ru-01 site could significantly reduce the ΔGH and thus improve the activity of HER. The calculated charge density differences in 2B doped alloy shown that the charge around the doped B atom increases, whereas the Ru-01 atom loses its charge (see in Figure S19). As a result, see in Figure 4B, the d-band center of Ru-4d in 2B doped alloy (−2.204 eV) moves far away from the Fermi level compared with the d-band center of Ru-4d in pure alloy (−1.932 eV). In conclusion, 2-B doping in alloy could gain charge from the surface Ru-01 atom, the charge loss of surface Ru-01 atom lead to the d-band center of Ru-4d moves far away from the Fermi level, and thus weakened the ΔGH and improved the HER performance of alloy.

Conclusion

In this research, B- and N-doped HEA porous carbon nanofibers with an *in situ* dendritic structure were fabricated for the first time. The growth process of the dendritic fibers and their impact on electrochemical properties were meticulously analyzed. The dendritic structure can offer more contact sites, and the carbon fiber-high entropy alloy combination can expedite electron and ion transport, thus diminishing the kinetic

reaction barrier. Doping with boron atoms can adjust the electron configuration and optimize hydrogen adsorption/desorption on the catalyst surface, enhancing the electrocatalytic efficiency. This study may guide the development of other borated HEA fibers and explore the use of dendritic fibers in various electrochemical applications.

Limitations of the study

The growth mechanism is complicated, and future research will focus on the growth mechanism of dendritic fiber and expand applications.

STAR★METHODS

Detailed methods are provided in the online version of this paper and include the following:

- KEY RESOURCES TABLE
- RESOURCE AVAILABILITY
  - Lead contact
  - Materials availability
  - Data and code availability
- METHOD DETAILS
  - Preparation of large-porosity HE-BN/PCNF
  - Instrumentation
  - Electrochemical characterization
  - Calculation method

SUPPLEMENTAL INFORMATION

Supplemental information can be found online at https://doi.org/10.1016/j.isci.2024.109616.

ACKNOWLEDGMENTS

This work was supported by the National Natural Science Foundation of China (52273077, 22103045, and 11904193), and State Key Laboratory of Bio-Fibers and Eco-Textiles, Qingdao University (RZ2000003334, ZDKT202108 and G2RC202022).

AUTHOR CONTRIBUTIONS

Conceptualization, J.L. and J.Z. (author 2); methodology, J.L. and M.N.; investigation, J.Z. (author 2), Y.L., and J.Z. (author 11_; measurements, J.L., X.L., Z.G., P.W., R.W., and S.W.; writing – original draft, J.L.; writing – review and editing, J.L., J.Z. (author 2), and Y.L.; funding acquisition, S.R. and Y.L.; supervision, J.Z. (author 2) and Y.L.

DECLARATION OF INTERESTS

The authors declare no competing interests.

Received: February 1, 2024
Revised: March 13, 2024
Accepted: March 26, 2024
Published: March 28, 2024

REFERENCES

1. Yao, Y., Dong, Q., Brozena, A., Luo, J., Miao, J., Chi, M., Wang, C., Kevrekidis, I.G., Ren, Z.J., Greeley, J., et al. (2022). High-entropy nanoparticles: Synthesis-structure-property relationships and data-driven discovery. Science *376*, eabn3103. https://doi.org/10.1126/science.abn3103.
2. Zhong, M., Xu, M., Ren, S., Li, W., Wang, C., Gao, M., and Lu, X. (2024). Modulating the electronic structure of $Ni(OH)_2$ by coupling with low-content Pt for boosting the urea oxidation reaction enables significantly promoted energy-saving hydrogen production. Energy Environ. Sci. *17*, 1984–1996. https://doi.org/10.1039/d3ee03398h.
3. Chen, X., Li, W., Wang, C., and Lu, X. (2023). Wet chemical synthesis of rhodium nanoparticles anchored on cobalt/nitrogen-doped carbon nanofibers for high-performance alkaline and acidic hydrogen evolution. J. Colloid Interface Sci. *650*, 304–312. https://doi.org/10.1016/j.jcis.2023.06.189.
4. Suen, N.T., Hung, S.F., Quan, Q., Zhang, N., Xu, Y.J., and Chen, H.M. (2017). Electrocatalysis for the oxygen evolution reaction: recent development and future perspectives. Chem. Soc. Rev. *46*, 337–365. https://doi.org/10.1039/c6cs00328a.
5. Chen, H.Y., Yang, L., Wang, R.X., Zhang, W.J., Liu, R., Yun, Y.Z., Wang, N., Ramakrishna, S., Jiao, L., and Long, Y.Z. (2023). Constructing CoO/Mo_2C Heterostructures with Interfacial Electron Redistribution Induced by Work Functions for Boosting Overall Water Splitting. Small *19*, e2304086. https://doi.org/10.1002/smll.202304086.
6. Yang, L., Cao, X., Wang, X., Wang, Q., and Jiao, L. (2023). Regulative electronic redistribution of $CoTe_2$/CoP heterointerfaces for accelerating water splitting. Appl. Catal. B Environ. *329*, 122551. https://doi.org/10.1016/j.apcatb.2023.122551.
7. Zhu, J., Hu, L., Zhao, P., Lee, L.Y.S., and Wong, K.Y. (2020). Recent Advances in Electrocatalytic Hydrogen Evolution Using Nanoparticles. Chem. Rev. *120*, 851–918. https://doi.org/10.1021/acs.chemrev.9b00248.
8. Li, W., Liu, R., Yu, G., Chen, X., Yan, S., Ren, S., Chen, J., Chen, W., Wang, C., and Lu, X.

(2023). Rationally Construction of Mn-Doped RuO_2 Nanofibers for High-Activity and Stable Alkaline Ampere-Level Current Density Overall Water Splitting. Small, e2307164. https://doi.org/10.1002/smll.202307164.

9. Zhong, M., Yang, J., Xu, M., Ren, S., Chen, X., Wang, C., Gao, M., and Lu, X. (2024). Significantly Enhanced Energy-Saving H_2 Production Coupled with Urea Oxidation by Low- and Non-Pt Anchored on NiS-Based Conductive Nanofibers. Small *20*, e2304782. https://doi.org/10.1002/smll.202304782.
10. Shi, H., Sun, X.Y., Liu, Y., Zeng, S.P., Zhang, Q.H., Gu, L., Wang, T.H., Han, G.F., Wen, Z., Fang, Q.R., et al. (2023). Multicomponent Intermetallic Nanoparticles on Hierarchical Metal Network as Versatile Electrocatalysts for Highly Efficient Water Splitting. Adv. Funct. Mater. *33*, 2214412. https://doi.org/10.1002/adfm.202214412.
11. Zhang, Y., Gao, F., Wang, D., Li, Z., Wang, X., Wang, C., Zhang, K., and Du, Y. (2023). Amorphous/Crystalline Heterostructure Transition-Metal-based Catalysts for High-Performance Water Splitting. Coord. Chem. Rev. *475*, 214916. https://doi.org/10.1016/j.ccr.2022.214916.
12. Wang, Y., Luo, W., Gong, S., Luo, L., Li, Y., Zhao, Y., and Li, Z. (2023). Synthesis of High-Entropy Alloy Nanoparticles by Step-Alloying Strategy as Superior Multifunctional Electrocatalyst. Adv. Mater. *35*, e2302499. https://doi.org/10.1002/adma.202302499.
13. Xin, Y., Li, S., Qian, Y., Zhu, W., Yuan, H., Jiang, P., Guo, R., and Wang, L. (2020). High-Entropy Alloys as a Platform for Catalysis: Progress, Challenges, and Opportunities. ACS Catal. *10*, 11280–11306. https://doi.org/10.1021/acscatal.0c03617.
14. Fan, M., Liang, X., Li, Q., Cui, L., He, X., and Zou, X. (2023). Boron: A key functional component for designing high-performance heterogeneous catalysts. Chin. Chem. Lett. *34*, 107275. https://doi.org/10.1016/j.cclet.2022.02.080.
15. Wu, H., Lu, Q., Li, Y., Zhao, M., Wang, J., Li, Y., Zhang, J., Zheng, X., Han, X., Zhao, N., et al. (2023). Structural Framework-Guided Universal Design of High-Entropy Compounds for Efficient Energy Catalysis. J. Am. Chem. Soc. *145*, 1924–1935. https://doi.org/10.1021/jacs.2c12295.
16. Tao, L., Sun, M., Zhou, Y., Luo, M., Lv, F., Li, M., Zhang, Q., Gu, L., Huang, B., and Guo, S. (2022). A General Synthetic Method for High-Entropy Alloy Subnanometer Ribbons. J. Am. Chem. Soc. *144*, 10582–10590. https://doi.org/10.1021/jacs.2c03544.
17. Muravev, V., Parastaev, A., van den Bosch, Y., Ligt, B., Claes, N., Bals, S., Kosinov, N., and Hensen, E.J.M. (2023). Size of cerium dioxide support nanocrystals dictates reactivity of highly dispersed palladium catalysts. Science *380*, 1174–1179. https://doi.org/10.1126/science.adf9082.
18. Zheng, Y., Jiao, Y., Vasileff, A., and Qiao, S.Z. (2018). The Hydrogen Evolution Reaction in Alkaline Solution: From Theory, Single Crystal Models, to Practical Electrocatalysts. Angew. Chem., Int. Ed. Engl. *57*, 7568–7579. https://doi.org/10.1002/anie.201710556.
19. Moloudi, M., Noori, A., Rahmanifar, M.S., Shabangoli, Y., El-Kady, M.F., Mohamed, N.B., Kaner, R.B., and Mousavi, M.F. (2022). Layered Double Hydroxide Templated Synthesis of Amorphous NiCoFeB as a Multifunctional Electrocatalyst for Overall Water Splitting and Rechargeable Zinc–Air Batteries. Adv. Energy Mater. *13*, 2203002. https://doi.org/10.1002/aenm.202203002.
20. Feng, C., Wang, F., Liu, Z., Nakabayashi, M., Xiao, Y., Zeng, Q., Fu, J., Wu, Q., Cui, C., Han, Y., et al. (2021). A self-healing catalyst for electrocatalytic and photoelectrochemical oxygen evolution in highly alkaline conditions. Nat. Commun. *12*, 5980. https://doi.org/10.1038/s41467-021-26281-0.
21. Liu, R., Hou, L., Yue, G., Li, H., Zhang, J., Liu, J., Miao, B., Wang, N., Bai, J., Cui, Z., et al. (2022). Progress of Fabrication and Applications of Electrospun Hierarchically Porous Nanofibers. Adv. Fiber Mater. *4*, 604–630. https://doi.org/10.1007/s42765-022-00132-z.
22. Wang, X.-X., Yu, G.-F., Zhang, J., Yu, M., Ramakrishna, S., and Long, Y.-Z. (2021). Conductive polymer ultrafine fibers via electrospinning: Preparation, physical properties and applications. Prog. Mater. Sci. *115*, 100704. https://doi.org/10.1016/j.pmatsci.2020.100704.
23. Zhu, H., Sun, S., Hao, J., Zhuang, Z., Zhang, S., Wang, T., Kang, Q., Lu, S., Wang, X., Lai, F., et al. (2023). A high-entropy atomic environment converts inactive to active sites for electrocatalysis. Energy Environ. Sci. *16*, 619–628. https://doi.org/10.1039/d2ee03185j.
24. Liu, H., Zhang, S., Liu, L., Yu, J., and Ding, B. (2019). A Fluffy Dual-Network Structured Nanofiber/Net Filter Enables High-Efficiency Air Filtration. Adv. Funct. Mater. *29*, 1904108. https://doi.org/10.1002/adfm.201904108.
25. Zhang, K., Li, Z., Kang, W., Deng, N., Yan, J., Ju, J., Liu, Y., and Cheng, B. (2018). Preparation and characterization of tree-like cellulose nanofiber membranes via the electrospinning method. Carbohydr. Polym. *183*, 62–69. https://doi.org/10.1016/j.carbpol.2017.11.032.
26. Wang, X., Ding, B., Sun, G., Wang, M., and Yu, J. (2013). Electro-spinning/netting: A strategy for the fabrication of three-dimensional polymer nano-fiber/nets. Prog. Mater. Sci. *58*, 1173–1243. https://doi.org/10.1016/j.pmatsci.2013.05.001.
27. Lei, C., Chen, H., Cao, J., Yang, J., Qiu, M., Xia, Y., Yuan, C., Yang, B., Li, Z., Zhang, X., et al. (2018). FeN_4 Sites Embedded into Carbon Nanofiber Integrated with Electrochemically Exfoliated Graphene for Oxygen Evolution in Acidic Medium. Adv. Energy Mater. *8*, 1801912. https://doi.org/10.1002/aenm.201801912.
28. Yang, H., Chen, Z., Guo, P., Fei, B., and Wu, R. (2020). B-doping-induced amorphization of LDH for large-current-density hydrogen evolution reaction. Appl. Catal. B Environ. *261*, 118240. https://doi.org/10.1016/j.apcatb.2019.118240.
29. Hao, J., Zhuang, Z., Cao, K., Gao, G., Wang, C., Lai, F., Lu, S., Ma, P., Dong, W., Liu, T., et al. (2022). Unraveling the electronegativity-dominated intermediate adsorption on high-entropy alloy electrocatalysts. Nat. Commun. *13*, 2662. https://doi.org/10.1038/s41467-022-30379-4.
30. Akopov, G., Yeung, M.T., and Kaner, R.B. (2017). Rediscovering the Crystal Chemistry of Borides. Adv. Mater. *29*, 1604506. https://doi.org/10.1002/adma.201604506.
31. Zhang, R., Liu, H., Wang, C., Wang, L., Yang, Y., and Guo, Y. (2020). Electroless Plating of Transition Metal Boride with High Boron Content as Superior HER Electrocatalyst. ChemCatChem *12*, 3068–3075. https://doi.org/10.1002/cctc.202000315.
32. Lu, W., Liu, T., Xie, L., Tang, C., Liu, D., Hao, S., Qu, F., Du, G., Ma, Y., Asiri, A.M., and Sun, X. (2017). In Situ Derived Co-B Nanoarray: A High-Efficiency and Durable 3D Bifunctional Electrocatalyst for Overall Alkaline Water Splitting. Small *13*, 1700805. https://doi.org/10.1002/smll.201700805.
33. Yu, X., Han, P., Wei, Z., Huang, L., Gu, Z., Peng, S., Ma, J., and Zheng, G. (2018). Boron-Doped Graphene for Electrocatalytic N_2 Reduction. Joule *2*, 1610–1622. https://doi.org/10.1016/j.joule.2018.06.007.
34. Wang, S., Ma, F., Jiang, H., Shao, Y., Wu, Y., and Hao, X. (2018). Band gap-Tunable Porous Borocarbonitride Nanosheets for High Energy-Density Supercapacitors. ACS Appl. Mater. Interfaces *10*, 19588–19597. https://doi.org/10.1021/acsami.8b02317.
35. Yang, M., Shi, D., Sun, X., Li, Y., Liang, Z., Zhang, L., Shao, Y., Wu, Y., and Hao, X. (2020). Shuttle confinement of lithium polysulfides in borocarbonitride nanotubes with enhanced performance for lithium–sulfur batteries. J. Mater. Chem. A Mater. *8*, 296–304. https://doi.org/10.1039/c9ta11500e.
36. Zhang, N., Cao, L., Feng, L., Huang, J., Kajiyoshi, K., Li, C., Liu, Q., Yang, D., and He, J. (2019). Co,N-Codoped porous vanadium nitride nanoplates as superior bifunctional electrocatalysts for hydrogen evolution and oxygen reduction reactions. Nanoscale *11*, 11542–11549. https://doi.org/10.1039/c9nr02637a.
37. Li, Z., Xue, K.H., Wang, J., Li, J.G., Ao, X., Sun, H., Song, X., Lei, W., Cao, Y., and Wang, C. (2020). Cation and Anion Co-doped Perovskite Nanofibers for Highly Efficient Electrocatalytic Oxygen Evolution. ACS Appl. Mater. Interfaces *12*, 41259–41268. https://doi.org/10.1021/acsami.0c10045.
38. Zhang, Z., Cai, J., Zhu, H., Zhuang, Z., Xu, F., Hao, J., Lu, S., Li, H., Duan, F., and Du, M. (2020). Simple construction of ruthenium single atoms on electrospun nanofibers for superior alkaline hydrogen evolution: A dynamic transformation from clusters to single atoms. Chem. Eng. J. *392*, 123655. https://doi.org/10.1016/j.cej.2019.123655.
39. Zhang, Z., Zhang, T., and Lee, J.Y. (2018). Enhancement Effect of Borate Doping on the Oxygen Evolution Activity of α-Nickel Hydroxide. ACS Appl. Nano Mater. *1*, 751–758. https://doi.org/10.1021/acsanm.7b00210.
40. Li, Y., Huang, B., Sun, Y., Luo, M., Yang, Y., Qin, Y., Wang, L., Li, C., Lv, F., Zhang, W., and Guo, S. (2019). Multimetal Borides Nanochains as Efficient Electrocatalysts for Overall Water Splitting. Small *15*, 1804212. https://doi.org/10.1002/smll.201804212.

STAR★METHODS

KEY RESOURCES TABLE

REAGENT or RESOURCE	SOURCE	IDENTIFIER
Chemicals, peptides, and recombinant proteins		
Anhydrous ferric trichloride	Shanghai Aladdin Biochemical Technology Co., Ltd.	CAS#7705-08-0
Nickel chloride hexahydrate	Shanghai Aladdin Biochemical Technology Co., Ltd.	CAS#7718-54-9
Cobalt chloride hexahydrate	Shanghai Aladdin Biochemical Technology Co., Ltd.	CAS#7791-13-1
Ruthenium chloride trihydrate	Shanghai Aladdin Biochemical Technology Co., Ltd.	CAS#14898-67-0
Manganese chloride tetrahydrate	Shanghai Aladdin Biochemical Technology Co., Ltd.	CAS#13446-34-9
Polyacrylonitrile	Shanghai Aladdin Biochemical Technology Co., Ltd.	CAS#25014-41-9
Poly(methyl methacrylate)	Shanghai Aladdin Biochemical Technology Co., Ltd.	CAS#9011-14-7
Boric acid	Shanghai Aladdin Biochemical Technology Co., Ltd.	CAS#10043-35-3
N, N-dimethylformamide	Shanghai Aladdin Biochemical Technology Co., Ltd.	CAS#68-12-2
Nafion	Shanghai Aladdin Biochemical Technology Co., Ltd.	CAS#31175-20-9
Potassium hydroxide	Shanghai Macklin Biochemical Technology Co., Ltd.	CAS# 1310-58-3

RESOURCE AVAILABILITY

Lead contact

Further information and requests for resources and reagents should be directed to and will be fulfilled by the lead contact, Yun-Ze Long (yunze.long@qdu.edu.cn).

Materials availability

No new reagents were created in the presented research.

Data and code availability

- All data reported in this paper will be shared by the lead contact upon request.
- This paper does not report original code.
- Any additional information required to reanalyze the data reported in this paper is available from the lead contact upon request.

METHOD DETAILS

Preparation of large-porosity HE-BN/PCNF

A mixture of 0.5 mmol of $MnCl_2{\cdot}4H_2O$ (0.099 g), 0.5 mmol of $FeCl_3$ (0.081 g), 0.5 mmol of $CoCl_2{\cdot}6H_2O$ (0.119 g), 0.5 mmol of $NiCl_2{\cdot}6H_2O$ (0.1188 g), and 0.5 mmol of $RuCl_3{\cdot}3H_2O$ (0.1037 g) was prepared. Additionally, 1.5 g of PMMA, 1.5 g of PAN, and varying amounts of boric acid were dissolved in 22 g of dimethylformamide (DMF). The mixture was magnetically stirred to form a homogeneous solution. The weights of boric acid used were 0, 0.1, 0.25, 0.65. 0.75 and 0.9 g, respectively. The spinning solution was loaded into a 5 mL syringe for electrospinning. The voltage between the nozzle and the receiver was set to 20 kV, the flow rate of the spinning solution was 15 μL min^{-1} and the distance between the receiver and the nozzle was 18 cm. Subsequently, the nanofibers were pre-oxidized at 230°C with a heating rate of 2°C min^{-1} for 3 h and carbonized at 1000°C for 3 h in a nitrogen atmosphere at the same heating rate. Finally, the as-synthesized FeCoNiMnRu-BN-porous carbon nanofibers were labeled as HE-B_0N/PCNF, HE-B_{10}N/PCNF, HE-B_{25}N/PCNF, HE-B_{65}N/PCNF, HE-B_{75}N/PCNF, and HE-B_{90}N/PCNF.

Instrumentation

Field-emission scanning electron microscopy (FE-SEM, Sigma 500) fitted with energy dispersive X-ray (EDX, Oxford), and transmission electron microscopy (TEM, FEI Tecnai G2F20) were used to investigate the morphologies and structures of HE-BN/PCNF. The crystal structure and elemental composition were characterized by powder XRD using Kα radiation (λ = 1.5406 Å) from 10° to 80°, and X-ray photoelectron spectroscopy (XPS, ESCALAB Xi+).

Electrochemical characterization

Electrochemical measurements were all conducted in a typical three-electrode system at 25°C in 1.0 M KOH using a CHI760E electrochemical station. Hg/HgO and a graphite rod were used as the reference electrode (RE) and count electrode (CE), respectively. The self-supported

CNFs-based materials were cut into 0.5 × 0.5 cm^2 and served as the working electrode (WE). Potentials were converted to the reversible hydrogen electrode (RHE) using the equation ERHE =0.0591 × pH + 0.098 V. Pt/C (20 wt%), the powder was taken as a control and deposited on a glassy carbon electrode (GCE) with a diameter of 5 mm for measurement. To prepare the electrocatalyst ink, 5 mg of electrocatalyst was dispersed into 0.485 mL of deionized water and 0.485 mL of ethanol mixed with 30 μL of Nafion117 solution. After another 30 min of ultrasonication, 5 μL of the electrocatalyst ink was cast on the GCE and dried naturally in the air. All linear sweep voltammetry (LSV) curves were obtained at a scan rate of 5 mV s^{-1} with 90% iR-compensation. Tafel plots were obtained according to the Tafel equation:

$$\eta = a + b \log j \quad \text{(Equation 3)}$$

where η, b, and j represent the overpotential, Tafel slope, and current density, respectively. Electrochemical double layer capacitances (C_{dl}) were measured by analyzing the cyclic voltammetry (CV) curves at scan rates of 2, 4, 6, 8, 10, and 12 mV s^{-1} in the range of –0.05 to –0.15 V vs. Hg/HgO. By plotting Δi/2 ($\Delta i = i_p - i_n$, where i_p and i_n represent the positive and negative current, respectively), the Cdl can be calculated using the equation: C_{dl} = Δi/2 v. Electrochemical active surface area (ECSA) was estimated by the equation: ECSA = Cdl/Cs, where the specific capacitance value (Cs) was taken as 0.04 mF cm^{-2}. The ECSA-normalized LSV curves were acquired using the equation: j_{ECSA} = i/ECSA, where j_{ECSA} and i represent the current density normalized to ECSA and the current of the working electrode, respectively. Chronoamperometry was performed to evaluate the durability of the samples.

Calculation method

The DFT calculations were carried out using the Vienna Ab-initio Simulation Package (VASP) with the frozen-core all-electron projector-augment-wave (PAW) method. The Perdew-Burke-Ernzerhof (PBE) of generalized gradient approximation (GGA) was adopted to describe the exchange and correlation potential. The cutoff energy for the plane-wave basis set was set to 450 eV. A 5-layer 3×3 Fe(111) slab (180 Fe atoms) was used, and a vacuum region of 15 Å above them was used to ensure the decoupling between neighboring systems. 145 Fe atoms in Fe(111) slab were randomly replaced by 44 Co, 40 Ni, 15 Mn, and 46 Ru atoms to build the model of pure alloy ($Fe_{35}Co_{44}Ni_{40}Mn_{15}Ru_{46}$). The B-doped alloy was simulated by inserting B atoms between the surface and sub-surface of $Fe_{35}Co_{44}Ni_{40}Mn_{15}Ru_{46}$. The geometry optimizations were performed until the forces on each ion was reduced below 0.01 eV/Å, and a 1×2×1 Monkhorst-Pack k-point sampling of the Brillouin zone was used. The DFT-D3 method were used to describe the van der Waals interaction.

The Gibbs free-energy (Δ*G*) is calculated as

$$\Delta G = EDFT + \Delta EZPE - T\Delta S \quad \text{(Equation 4)}$$

ΔE_{ZPE} is the difference corresponding to the zero point energy between the adsorbed molecule and molecule in the gas phase and Δ*S* is one molecule entropy between absorbed state and gas phase. *E*DFT is the total energy of DFT calculated system.